

Unique surface-state connection between Weyl and nodal ring fermions in ferromagnetic material Cs_2MoCl_6

Tiantian Zhang,^{1,2,*} Daisuke Hara,^{1,†} and Shuichi Murakami^{1,2}

¹*Department of Physics, Tokyo Institute of Technology, Ookayama, Meguro-ku, Tokyo 152-8551, Japan*

²*Tokodai Institute for Element Strategy, Tokyo Institute of Technology, Nagatsuta, Midori-ku, Yokohama, Kanagawa 226-8503, Japan*

For topological materials with coexistence of Weyl nodes and nodal rings, the surface-state configuration and connection are unique yet have never been studied and discussed before. In this paper, we predict a ferromagnetic (FM) material, Cs_2MoCl_6 , with coexistence of Weyl and nodal ring fermions in its spinful FM electronic band structure, which is unusual since FM materials are very rare in nature and node-ring band crossings will usually open a gap when spin-orbit coupling (SOC) is taken into consideration. We find that the surface states of Cs_2MoCl_6 show different properties along different directions, i.e., the surface states are in the drumhead shape showing the node-ring property on the (001) surface and in the helicoid shape showing the Weyl property on the (010) surface. Interestingly, both the drumhead surface states and the helicoid surface states will cross the projected points of the Weyl and nodal ring along different directions. In particular, helicoid surface states on the (010) surface will meet the nodal ring tangentially, with their shapes change abruptly as a function of the energy. We implement both first-principle calculation and an analytical model to understand the unique surface-state connection for systems with the coexistence of Weyl nodes and nodal rings (or nodal lines). This result is universal and irrespective of the presence/absence of and time-reversal symmetry (\mathcal{T}).

Introduction In the recent years, topological magnetic materials [1–17] draw much attention due to their exotic properties, *e.g.*, topological axion insulator states [18–20], intrinsic quantum anomalous Hall effect without external magnetic fields [6, 7, 9, 11–13], and the display of magnetism, topology, spin dynamics and quantum transport. However, experimentally synthesized and verified magnetic topological materials are very limited, especially for the magnetic topological semimetals [8, 10–16]. Furthermore, compared to the bulk topology, properties of topological surface states like the configuration and connection are not so well understood in some systems. In this paper, we propose a “high-quality” FM material Cs_2MoCl_6 [21] with space group $Fm\bar{3}m$ that have both Weyl and node-ring fermions in its spinful electronic band structure. We find unique surface-state connection between the Weyl and node-ring fermions along different surface directions by both DFT and model analysis due to an intriguing interplay between drumhead surface states (DSSs) from nodal rings and helicoid surface states (HSSs), i.e., Fermi-arc surface states, from Weyl nodes. We show that the DSSs always go across the Weyl nodes, when the projection of the Weyl nodes are inside that of the nodal ring. We also show that how the HSSs connect the projection of the nodal ring and the curvature of HSSs depend sensitively on the energy. Such unique surface-state connection also appear in several previous studies, yet lack of discussion [22–26]. Our results show that the connection pattern of the surface states is surface-dependent for systems with both Weyl and node-ring fermions, and it is universal for systems with/without considering SOC and \mathcal{T} symmetry.

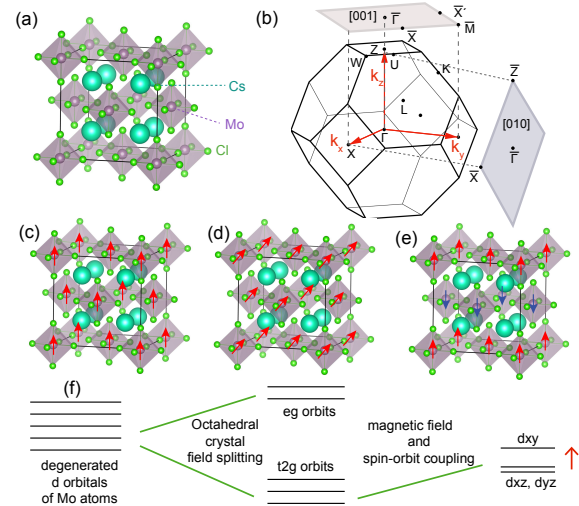


FIG. 1. Crystal structure, Brillouin zone and splitting of d orbitals of Cs_2MoCl_6 . (a-b) are the crystal structure and (surface) Brillouin zone of Cs_2MoCl_6 . (c-e) are three different types of magnetic structure of Cs_2MoCl_6 with ferromagnetic phase along [001] direction, [111] direction and antiferromagnetic phase, respectively. (f) shows the splitting of d orbitals under different fields.

Crystal and magnetic structure for Cs_2MoCl_6 Cs_2MoCl_6 belongs to space group #225, and the lattice constant we use in this paper is $a = 10.57 \text{ \AA}$ after a relaxation on atomic positions, which is slightly different from the experimental data 10.21 \AA at room temperature [21]. For most of the compounds having a similar crystal structure with Cs_2MoCl_6 (*e.g.*, replacing Cs, Mo and Cl by other alkali metal elements, transition metal elements

and halogen elements, respectively), their magnetic properties have not been explored by experiments except for Cs_2CoF_6 and Rb_2CoF_6 , which have a FM phase at low temperature [27], and Cs_2MoCl_6 is also among the ones lacking of exploration.

In order to explore the magnetic structure of the ground state in Cs_2MoCl_6 , we calculate the total energy of the systems with three different magnetic structures for #225 by DFT, which are shown in Fig. 1 (c-e). The total energy for the FM phase in Fig. 1 (c) and (d) is about 20 meV lower than the antiferromagnetic phase in Fig. 1 (e) per unit cell, and the FM phase with magnetic order on the (001) surface (Fig. 1 (c)) will have a smaller total energy about 1 meV per unit cell than that along [111] direction (Fig. 1 (d)). Thus, we will choose the one with magnetic moment along the highest symmetry direction, i.e., [001] direction to explore the topological properties in Cs_2MoCl_6 . In the following, we will introduce topology of the electronic band structure of Cs_2MoCl_6 both in the nonmagnetic (NM) phase and in the FM phase separately.

Band structure of Cs_2MoCl_6 In the spinless NM electronic band structure, d orbitals from Mo will split into e_g and t_{2g} orbitals due to the octahedral crystal field environment and the splitting is very huge due to the large $p-d$ hybridization of Mo and Cl , as shown in Fig. 1 (f) and Fig. 2 (a). Thus, we only need to study the t_{2g} orbitals located near the Fermi energy and they exhibit nontrivial topologies, i.e., nodal chains formed by the two lowest t_{2g} orbitals crossing the Fermi level. Due to the existence of mirror symmetries, all the nodal rings will be pinned on the M_x , M_y and M_z planes, and meet with each other at the high-symmetry point W , forming a nodal chain semimetal, as shown in Figs. 2 (b-c).

Figure 3 (a) show the spinful electronic band structure of Cs_2MoCl_6 with FM phase by DFT+ U method [28], and the Hubbard U term for Mo is 0.33 eV obtained by the linear response method [29]. After considering the FM structure with magnetic moment on the (001) surface and SOC, M_z and C_{4z} will still be preserved, while $M_{x,y}$ and $C_{4x,4y}$ will be broken. Thus, the nodal chain on the $M_{x,y}$ plane will open a gap but still leave a single nodal ring protected by the M_z symmetry. However, the nodal ring will move slightly away from W point due to the symmetry breaking, and cross the high-symmetry line $W_1 - W_2$ as shown in Fig. 3 (b). Furthermore, SOC will make a change on the band structure along Γ - Z direction, and generate a pair of Weyl points protected by the C_{4z} symmetry, as shown by the red and green hexagons in Fig. 3 (b). Therefore, the t_{2g} bands will be significantly affected after considering the FM order and SOC, which make the nodal chains into a pair of Weyl points and a single nodal ring, as shown in Fig. 3 (b).

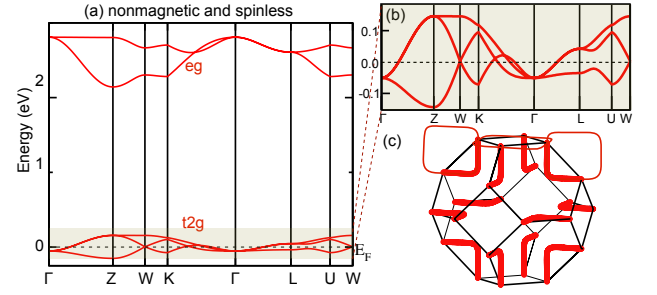


FIG. 2. Spinless electronic band structure and the nodal chain distribution of Cs_2MoCl_6 in the NM phase. (a) is the spinless electronic band structure of Cs_2MoCl_6 in the NM phase, where the t_{2g} orbitals are magnified in (b). (c) shows the nodal chain band crossing formed by the lowest two bands of t_{2g} orbitals.

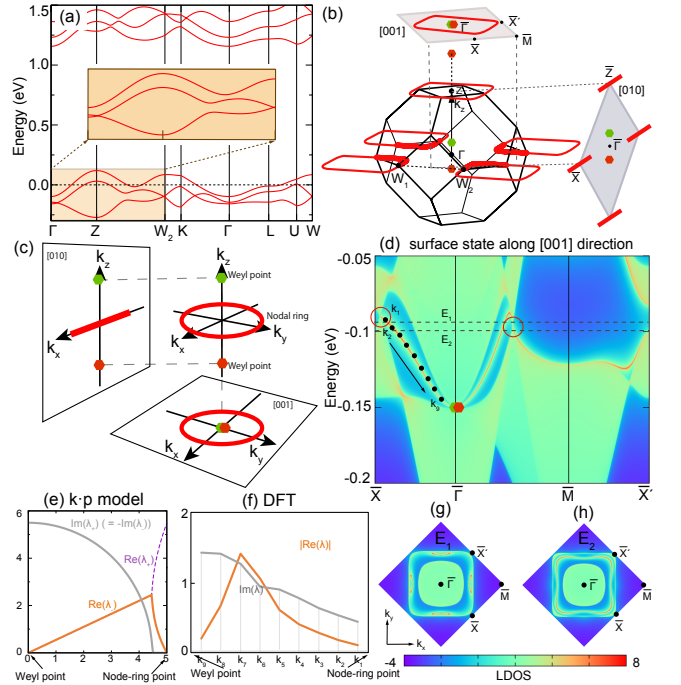


FIG. 3. Spinful electronic band structure and topological calculations on Cs_2MoCl_6 in the FM phase. (a) is the spinful electronic band structure of Cs_2MoCl_6 in the FM phase with magnetic moment along [001] direction. (b) show the positions of a pair of Weyl points (red and green hexagons) and nodal rings in the bulk, (001) and (010) surface BZ. (c) Schematic figure of the projected positions of the nodal ring and Weyl points on the (001) and (010) surfaces. (d) is the surface states, together with the projection of the Weyl points (red and green hexagons) and the nodal ring (red circles) on the (001) surface. (e) is the real and imaginary parts for λ_+ obtained by the $k \cdot p$ model with parameters of $\bar{D} = 1$ and $\sqrt{m} = 5$, where $\text{Im}(\lambda_-) = -\text{Im}(\lambda_+)$. (f) is the absolute value of the real part $|\text{Re}(\lambda)|$ and the imaginary part $\text{Im}(\lambda)$ obtained by the DFT calculation, where the k points are labelled in (d). (g-h) are the DSSs with different energies labelled in (d), where E_1 corresponds to the energy of nodal rings.

k · p model analysis Since two bands forming the Weyl points and a nodal ring are well separated from other bands, an effective 2×2 Hamiltonian based on the basis set $\{d_{xz}, d_{yz}\}$ can be constructed to describe the topological and other physical properties of the system. As discussed above, SOC and FM order will break the spin-rotation symmetry, $M_{x,y}$ and $C_{4x,4y}$ of the system, reducing the symmetry of the system to C_{4h} . Furthermore, the eigenvalues of the \hat{C}_{4z} operator for those two bands along Γ -Z direction are $e^{-\frac{\pi i}{4}}$ and $e^{\frac{3\pi i}{4}}$, so the $k \cdot p$ Hamiltonian describing the system around Z with C_{4h} double group symmetry can be written to the lowest order in \mathbf{k} as:

$$H(k_x, k_y, k_z) = \begin{pmatrix} m - |\mathbf{k}|^2 & \tilde{D}k_z k_+ \\ \tilde{D}k_z k_- & -m + |\mathbf{k}|^2 \end{pmatrix}, \quad (1)$$

where $k_{\pm} = k_x \pm ik_y$ and \mathbf{k} is a wavevector measured from the Z point. \tilde{D} and m are positive constants. We derived this Hamiltonian from the irreducible representations of the two bands around Z after proper rescaling of the wavevector (see the Supplementary Material for details [30]). Eigenvalues of H are $E = \pm \sqrt{(m - |\mathbf{k}|^2)^2 + \tilde{D}^2 k_z^2 (k_x^2 + k_y^2)}$, which form a pair of Weyl points and a single nodal ring located at ($k_x = 0, k_y = 0, k_z = \pm \sqrt{m}$) and ($k_x^2 + k_y^2 = m, k_z = 0$) with $E = 0$, respectively, as shown in Fig. 3 (c).

As you may notice, the projections of topological band crossings on different surfaces will have different configurations. Namely, the two Weyl points will be projected inside of the nodal ring on the (001) surface, and to different sides of the projection of the nodal ring on the (010) surface (Fig. 3 (c)). This difference will lead to different types of surface-state connection, which will be explored by both DFT calculation and model analysis in the following. Topological surface states obtained by DFT are calculated by the Green's function method [31, 32] with the tight-binding Hamiltonian obtained from maximally localized Wannier functions [33, 34].

Surface states of FM Cs₂MoCl₆ on the (001) surface Figure 3 (d) shows the surface states on the (001) surface, where two Weyl points will be projected onto the center of the nodal ring, i.e., $\bar{\Gamma}$, as shown in Fig. 3 (b). It is worth to mention that the topological surface states as well as the bulk bands are fully spin-polarized in Cs₂MoCl₆. In order to get a better understanding of the surface states connection and configuration, we also calculate the Fermi arcs with different energies, as shown in Figs. 3 (g-h). The calculations show that the surface states on the (001) surface are in a drumhead shape, which is the characteristic of the nodal ring semimetal, and they will cross the projection of the Weyl points for systems with coexistence of Weyl points and a nodal ring. Thus, we can control the density of the surface states or the Fermi velocity of the topological surface states on the (001) surface by modulating the energy of Weyl points and nodal rings. In the following, we will also use the

analytical model for a further discussion on the universal connection pattern between a pair of Weyl points and a nodal ring.

According to the $k \cdot p$ model in Eq. (1), the nodal ring will be projected onto a circle $k_x^2 + k_y^2 = m$ and two Weyl points will be projected onto the $k_x = k_y = 0$ point on the (001) surface. In order to obtain the eigenvalues and eigenvectors of the surface states, we will deal with a semi-infinite system where the bulk and the vacuum lie in $z \leq 0$ and in $z > 0$, respectively. In this case, k_z is no longer a good quantum number, so we need to replace k_z by $-i\partial_z$ [35, 36] and obtain the Hamiltonian of the semi-infinite system:

$$H_z(k_x, k_y) = \begin{pmatrix} m - R^2 + \frac{\partial^2}{\partial z^2} & -i\tilde{D}R e^{i\theta} \frac{\partial}{\partial z} \\ -i\tilde{D}R e^{-i\theta} \frac{\partial}{\partial z} & -m + R^2 - \frac{\partial^2}{\partial z^2} \end{pmatrix}, \quad (2)$$

where $k_{\pm} = R e^{\pm i\theta}$ with $R(> 0)$ and θ being real. By introducing a trial wavefunction proportional to $e^{\lambda z}$ and a parameter λ satisfying $\text{Re}(\lambda) > 0$ to represent a surface state, we obtain the corresponding eigenvectors

$$\psi_{\pm}(z) = \begin{pmatrix} i\tilde{D}R e^{i\theta} \lambda_{\pm} \\ m - R^2 + \lambda_{\pm}^2 - E \end{pmatrix} e^{\lambda_{\pm} z}, \quad (3)$$

where $\lambda_{\pm}^2 = \frac{1}{2}\tilde{D}^2 R^2 - (m - R^2) \pm \sqrt{E^2 - (m - R^2)\tilde{D}^2 R^2 + \frac{1}{4}\tilde{D}^4 R^4}$. If we impose a boundary condition $\psi(z = 0) = 0$ for an eigenvector of the form $\psi = C_+ \psi_+ + C_- \psi_-$ (C_{\pm} : constant), we obtain dispersionless DSSs with $E = 0$, and λ_{\pm} becomes $\lambda_{\pm} = \frac{\tilde{D}R}{2} \pm \sqrt{\left(\frac{\tilde{D}R}{2}\right)^2 + R^2 - m}$ (see the Supplementary Material for details [30]). In order to meet the condition of $\text{Re}(\lambda) > 0$, R should satisfy $|R| \leq \sqrt{m}$. Therefore, the DSSs cross the projection of the Weyl points lying at $E = 0$, which match with our DFT calculations very well.

Next, we will study the penetration length for the surface states on the (001) surface, which have a unique connection between Weyl points and the nodal ring, by both the analytical model and DFT calculation separately. The penetration length l for a wave function proportional to $e^{\lambda z}$ ($\lambda = \lambda_{\pm}$) is given by $l_{\pm} = \frac{1}{\text{Re}(\lambda_{\pm})}$. Here, we consider l_- as the penetration depth because $l_- \geq l_+$. When the surface state approaches the Weyl points or the nodal ring, the penetration length l_- is expected to be divergent due to the bulk nature of these bands. Figure 3 (e) shows the values of λ_{\pm} as a function of R , which is between the projection of the Weyl points ($R = 0$) and the nodal ring ($R = \sqrt{m}$). We notice that $R = \tilde{R} = \sqrt{\frac{4m}{\tilde{D}^2 + 4}}$ is a special point in that $\lambda_+ = \lambda_-$ is satisfied and the behavior of l_{\pm} changes drastically. When $R > \tilde{R}$, λ_{\pm} are real and the surface state decays into the bulk without oscillation. On the other hand, when $R < \tilde{R}$, λ_{\pm} are complex and the surface states show an oscillating decay into the bulk. Further calculations obtained by a 47

layers' slab with the tight-binding Hamiltonian obtained from maximally localized Wannier functions also show the same trend with the model calculation for both the real and imaginary part of λ , which are shown in Fig. 3 (f).

Surface states of FM Cs_2MoCl_6 on the (010) surface
On the (010) surface, two Weyl points will be projected on the $\bar{\Gamma}$ - \bar{Z} high-symmetry line, while the nodal ring will be projected to a line near \bar{X} and \bar{Z} , as shown in Fig. 3 (b-c). Figures 4 (b-d) show the Fermi arcs with different energies labelled in Fig. 4 (a), where E_2 corresponds to the energy of the nodal ring projected at \bar{Z} . When the energy for the isoenergetic contour decreases from E_1 to E_3 , the Fermi arcs from Weyl points will cross through the projected points of the nodal ring, and rotate around two Weyl points. Thus, surface states on the (010) surface are in a helicoid shape and show the feature of Weyl points, which is different with the surface states on the (001) surface showing the feature of nodal ring.

This Fermi-arc surface states agrees with expectations from bulk quantities. At Γ point ($k_z = 0$), the Γ_6^+ ($C_4 = e^{-\frac{\pi i}{4}}$) irreducible representation has a lower energy than Γ_7^+ ($C_4 = e^{-\frac{3\pi i}{4}}$), and at the Z point ($k_z = \pi$), the Z_7^+ ($C_4 = e^{-\frac{3\pi i}{4}}$) irreducible representation has a lower energy than Z_6^+ ($C_4 = e^{-\frac{\pi i}{4}}$). From this band inversion between different C_4 eigenstates, we can derive the difference of Chern numbers ($Ch(k_z)$) between $k_z = 0$ and $k_z = \pi$ subspaces. From Ref. [37, 38], we get $\frac{i^{Ch(k_z=\pi-\delta)}}{i^{Ch(k_z=\delta)}} = \frac{e^{-\frac{3\pi i}{4}}}{e^{-\frac{\pi i}{4}}} = -i$. Namely, $Ch(k_z = \pi - \delta) - Ch(k_z = \delta) \equiv -1 \pmod{4}$. Here, δ is a small constant, which is introduced to make the spectrum gapped by avoiding the nodal ring. This difference of Chern numbers is caused by the Weyl nodes at $\mathbf{k} = (0, 0, \pm k_0)$ ($k_0 > 0$), with a monopole charge ∓ 1 , respectively. In the present case, $Ch(k_z) = 0$ for $0 < |k_z| < k_0$ and $Ch(k_z) = -1$ for $k_0 < |k_z| < \pi$, leading to topological chiral surface states with negative velocity v_x on the (010) surface. It perfectly agrees with Figs. 4 (b-d).

Further model calculations on the (010) surface also verify this point, as shown in Figs. 4 (e-g) (see the Supplementary Material for details [30]). The projection of the Weyl points and the nodal ring are located at $(k_x, k_z) = (0, \pm\sqrt{m})$ and $(k_z = 0, -\sqrt{m} \leq k_x \leq \sqrt{m})$, respectively. When $E = 0$ (Fig. 4(f)), the Fermi arcs cross the projected nodal ring and connect two Weyl points straightly; when $E > 0$ and $E < 0$ (Fig. 4(f) and (g)), Fermi arcs rotate around two Weyl points and cross through the nodal rings. Remarkably, when $E \neq 0$, the Fermi arc meets the nodal ring tangentially, and the direction of the Fermi arc near the nodal ring change abruptly across $E = 0$, as shown in Figs. 4(e-g). It is due to an interplay between the helicoid nature of the

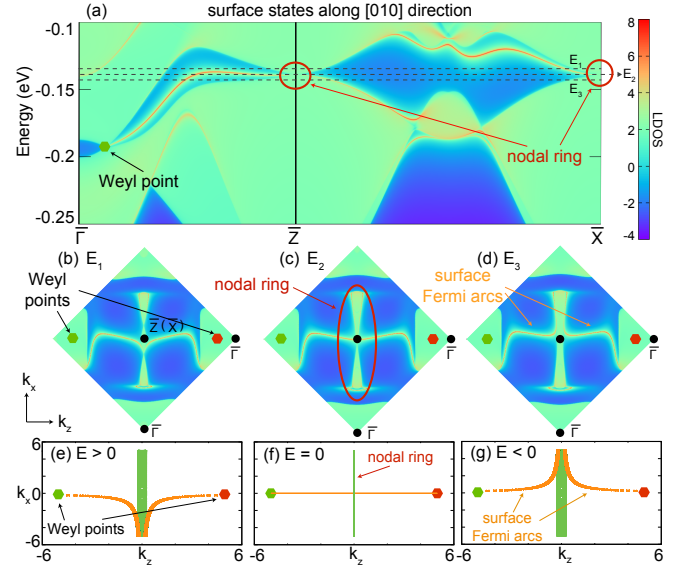


FIG. 4. Surface states calculation on the (010) surface for Cs_2MoCl_6 . (a) is the surface state on the (010) surface. (b-d) are the Fermi arcs with different energies labelled in (a), where E_2 corresponds to the energy of the nodal ring projected at \bar{Z} . (e-g) are Fermi arc calculations by the $k \cdot p$ model with $E > 0$, $E = 0$ and $E < 0$. Parameters are $\bar{D} = 1$ and $\sqrt{m} = 5$. The red and green hexagons represent the Weyl nodes with chiralities $+1$ (monopole) and -1 (antimonopole), respectively.

surface state and the tangential property between the surface Fermi arc and a bulk Fermi surface. This abrupt change of the Fermi arc also appears in Figs. 4(b-d) from the DFT. Both the DFT calculation and the model calculation on the Fermi arcs show perfect match with each other, which proves the correctness of our theory on the unique surface states connection.

We notice that such unique surface-state connection behavior can be found in other materials with different symmetries, such as in the electronic band structure of FM $HgCr_2Se_4$ (with SOC and without \mathcal{T}) [24], the electronic band structure of FM double perovskites (Ba_2NaOsO_6 , Sr_2SrOsO_6 , Ba_2ZnReO_6 , Ba_2MgReO_6 , and Ba_2CdReO_6 , with SOC and without \mathcal{T}) [22, 23], and the phonon band structure of oxide perovskites ($BaTiO_3$, $PbTiO_3$, without SOC and with \mathcal{T}) [26]. However, none of those works discuss on the connection of the unique surface states, and they mainly focus on the topology of the bulk bands. We demonstrate that both the drum-head surface states and the helicoid surface states will cross the projected points of the Weyl and nodal ring along different directions. Such surface-state connection for systems with the coexistence of Weyl points and nodal rings (and nodal lines) are universal, and it is also applicable to systems with/without considering SOC and \mathcal{T} .

Conclusion We propose a FM topological half metal Cs_2MoCl_6 with spin-polarized bulk bands and surface states near the Fermi level. Due to the coexistence

of Weyl points and a nodal ring, the surface states of Cs_2MoCl_6 show different properties along different directions. On the (001) surface, the surface states are in the drumhead shape, and it always go across the Weyl nodes. On the (010) surface, the Fermi-arc surface states are in a helicoid shape, and they meet the nodal ring tangentially, with their shapes change abruptly as a function of the energy. Analytical model calculation also match with the DFT calculation on both and surface states connection and configuration, which helps to verify our theory on the topological surface states. Such unique feature of the surface states connection is universal for systems with the coexistence of Weyl points and nodal rings, irrespective of the presence/absence of time-reversal symmetry and spin-orbit coupling.

Acknowledgements We acknowledge the supports from JSPS KAKENHI Grants No. JP18H03678 and No. JP20H04633, Tokodai Institute for Element Strategy (TIES) funded by MEXT Elements Strategy Initiative to Form Core Research Center. T. Z. also acknowledge the support by Japan Society for the Promotion of Science (JSPS), KAKENHI Grant No. JP21K13865.

* These two authors contributed equally;
zhang.t.ac@m.titech.ac.jp

† These two authors contributed equally

- [1] Jinyu Zou, Zhuoran He, and Gang Xu. The study of magnetic topological semimetals by first principles calculations. *npj Computational Materials*, 5(1):1–19, 2019.
- [2] Simin Nie, Gang Xu, Fritz B Prinz, and Shou-cheng Zhang. Topological semimetal in honeycomb lattice LnSi . *Proceedings of the National Academy of Sciences*, 114(40):10596–10600, 2017.
- [3] Run-Wu Zhang, Zeying Zhang, Cheng-Cheng Liu, and Yugui Yao. Nodal line spin-gapless semimetals and high-quality candidate materials. *Phys. Rev. Lett.*, 124:016402, Jan 2020.
- [4] Zhijun Wang, M. G. Vergniory, S. Kushwaha, Max Hirschberger, E. V. Chulkov, A. Ernst, N. P. Ong, Robert J. Cava, and B. Andrei Bernevig. Time-reversal-breaking Weyl fermions in magnetic Heusler alloys. *Phys. Rev. Lett.*, 117:236401, Nov 2016.
- [5] Simin Nie, Yan Sun, Fritz B. Prinz, Zhijun Wang, Hongming Weng, Zhong Fang, and Xi Dai. Magnetic semimetals and quantized anomalous Hall effect in EuB_6 . *Phys. Rev. Lett.*, 124:076403, Feb 2020.
- [6] Gang Xu, Hongming Weng, Zhijun Wang, Xi Dai, and Zhong Fang. Chern semimetal and the quantized anomalous Hall effect in HgCr_2Se_4 . *Phys. Rev. Lett.*, 107:186806, Oct 2011.
- [7] Jonathan Noky, Qiunan Xu, Claudia Felser, and Yan Sun. Large anomalous Hall and Nernst effects from nodal line symmetry breaking in Fe_2MnX ($X = \text{P, As, Sb}$). *Phys. Rev. B*, 99:165117, Apr 2019.
- [8] Ilya Belopolski, Kaustuv Manna, Daniel S Sanchez, Guoqing Chang, Benedikt Ernst, Jiaxin Yin, Songtian S Zhang, Tyler Cochran, Nana Shumiya, Hao Zheng, et al. Discovery of topological Weyl fermion lines and drumhead surface states in a room temperature magnet. *Science*, 365(6459):1278–1281, 2019.
- [9] Cui-Zu Chang, Jinsong Zhang, Xiao Feng, Jie Shen, Zuocheng Zhang, Minghua Guo, Kang Li, Yunbo Ou, Pang Wei, Li-Li Wang, et al. Experimental observation of the quantum anomalous Hall effect in a magnetic topological insulator. *Science*, 340(6129):167–170, 2013.
- [10] K Kuroda, T Tomita, M-T Suzuki, C Bareille, AA Nugroho, Pallab Goswami, M Ochi, M Ikhlas, M Nakayama, S Akebi, et al. Evidence for magnetic Weyl fermions in a correlated metal. *Nature Materials*, 16(11):1090–1095, 2017.
- [11] Kyoo Kim, Junho Seo, Eunwoo Lee, K-T Ko, BS Kim, Bo Gyu Jang, Jong Mok Ok, Jinwon Lee, Youn Jung Jo, Woun Kang, et al. Large anomalous Hall current induced by topological nodal lines in a ferromagnetic van der Waals semimetal. *Nature Materials*, 17(9):794–799, 2018.
- [12] Qi Wang, Yuanfeng Xu, Rui Lou, Zhonghao Liu, Man Li, Yaobo Huang, Dawei Shen, Hongming Weng, Shancai Wang, and Hechang Lei. Large intrinsic anomalous Hall effect in half-metallic ferromagnet $\text{Co}_3\text{Sn}_2\text{S}_2$ with magnetic Weyl fermions. *Nature Communications*, 9(1):1–8, 2018.
- [13] Peigang Li, Jahyun Koo, Wei Ning, Jinguo Li, Leixin Miao, Lujin Min, Yanglin Zhu, Yu Wang, Nasim Alem, Chao-Xing Liu, et al. Giant room temperature anomalous Hall effect and tunable topology in a ferromagnetic topological semimetal Co_2MnAl . *Nature Communications*, 11(1):1–8, 2020.
- [14] B. W. Xia, Y. J. Jin, J. Z. Zhao, Z. J. Chen, B. B. Zheng, Y. J. Zhao, R. Wang, and H. Xu. Robust twin pairs of Weyl fermions in ferromagnetic oxides. *Phys. Rev. Lett.*, 122:057205, Feb 2019.
- [15] Noam Morali, Rajib Batabyal, Pranab Kumar Nag, Enke Liu, Qiunan Xu, Yan Sun, Binghai Yan, Claudia Felser, Nurit Avraham, and Haim Beidenkopf. Fermi-arc diversity on surface terminations of the magnetic Weyl semimetal $\text{Co}_3\text{Sn}_2\text{S}_2$. *Science*, 365(6459):1286–1291, 2019.
- [16] DF Liu, AJ Liang, EK Liu, QN Xu, YW Li, C Chen, D Pei, WJ Shi, SK Mo, P Dudin, et al. Magnetic Weyl semimetal phase in a Kagomé crystal. *Science*, 365(6459):1282–1285, 2019.
- [17] Yuanfeng Xu, Luis Elcoro, Zhi-Da Song, Benjamin J Wieder, MG Vergniory, Nicolas Regnault, Yulin Chen, Claudia Felser, and B Andrei Bernevig. High-throughput calculations of magnetic topological materials. *Nature*, 586(7831):702–707, 2020.
- [18] Dongqin Zhang, Minji Shi, Tongshuai Zhu, Dingyu Xing, Haijun Zhang, and Jing Wang. Topological axion states in the magnetic insulator MnBi_2Te_4 with the quantized magnetoelectric effect. *Phys. Rev. Lett.*, 122:206401, May 2019.
- [19] Yuanfeng Xu, Zhida Song, Zhijun Wang, Hongming Weng, and Xi Dai. Higher-order topology of the axion insulator EuIn_2As_2 . *Physical review letters*, 122(25):256402, 2019.
- [20] Jiaheng Li, Yang Li, Shiqiao Du, Zun Wang, Bing-Lin Gu, Shou-Cheng Zhang, Ke He, Wenhui Duan, and Yong Xu. Intrinsic magnetic topological insulators in van der Waals layered MnBi_2Te_4 -family materials. *Science Advances*, 5(6):eaaw5685, 2019.

- [21] B Hu, P Wang, Y Xiao, and L-P Song. Crystal structure of dicesium hexachloromolybdate (IV), $\text{Cs}_2[\text{MoCl}_6]$. *Zeitschrift für Kristallographie-New Crystal Structures*, 220(1-4):318–318, 2005.
- [22] Young-Joon Song and Kwan-Woo Lee. Symmetry-protected spinful magnetic Weyl nodal loops and multi-Weyl nodes in $5d^n$ cubic double perovskites ($n=1, 2$). *Physical Review B*, 102(3):035155, 2020.
- [23] Xinlei Zhao, Peng-jie Guo, Fengjie Ma, and Zhong-Yi Lu. Coexistence of topological Weyl and nodal-ring states in ferromagnetic and ferrimagnetic double perovskites. *Physical Review B*, 103(8):085138, 2021.
- [24] Gang Xu, Hongming Weng, Zhijun Wang, Xi Dai, and Zhong Fang. Chern semimetal and the quantized anomalous Hall effect in HgCr_2Se_4 . *Physical Review Letters*, 107(18):186806, 2011.
- [25] Xiao-Qi Sun, Shou-Cheng Zhang, and Tomáš Bzdušek. Conversion rules for Weyl points and nodal lines in topological media. *Physical Review Letters*, 121(10):106402, 2018.
- [26] Bo Peng, Yuchen Hu, Shuichi Murakami, Tiantian Zhang, and Bartomeu Monserrat. Topological phonons in oxide perovskites controlled by light. *Science Advances*, 6(46):eabd1618, 2020.
- [27] JW Quail and GA Rivett. Complex fluorides of tetravalent cobalt. *Canadian Journal of Chemistry*, 50(15):2447–2450, 1972.
- [28] S. L. Dudarev, G. A. Botton, S. Y. Savrasov, C. J. Humphreys, and A. P. Sutton. Electron-energy-loss spectra and the structural stability of nickel oxide: An LSDA+U study. *Phys. Rev. B*, 57:1505–1509, Jan 1998.
- [29] Matteo Cococcioni and Stefano de Gironcoli. Linear response approach to the calculation of the effective interaction parameters in the LDA + U method. *Phys. Rev. B*, 71:035105, Jan 2005.
- [30] See Supplementary Material at [] for (i) density of states for nonmagnetic Cs_2MoCl_6 , (ii) electronic band structure for Cs_2MoCl_6 with different magnetic orders, (iii) derivation of the effective model, (iv) surface states calculations on the (001) surface by $k \cdot p$ model and (v) surface states calculations on the (010) surface by $k \cdot p$ model.
- [31] MP Lopez Sancho, JM Lopez Sancho, and Jessy Rubio. Quick iterative scheme for the calculation of transfer matrices: application to Mo (100). *Journal of Physics F: Metal Physics*, 14(5):1205, 1984.
- [32] QuanSheng Wu, ShengNan Zhang, Hai-Feng Song, Matthias Troyer, and Alexey A Soluyanov. Wanniertools: An open-source software package for novel topological materials. *Computer Physics Communications*, 224:405–416, 2018.
- [33] Arash A Mostofi, Jonathan R Yates, Young-Su Lee, Ivo Souza, David Vanderbilt, and Nicola Marzari. wannier90: A tool for obtaining maximally-localised Wannier functions. *Computer Physics Communications*, 178(9):685–699, 2008.
- [34] Nicola Marzari, Arash A. Mostofi, Jonathan R. Yates, Ivo Souza, and David Vanderbilt. Maximally localized Wannier functions: Theory and applications. *Rev. Mod. Phys.*, 84:1419–1475, Oct 2012.
- [35] Bin Zhou, Hai-Zhou Lu, Rui-Lin Chu, Shun-Qing Shen, and Qian Niu. Finite size effects on helical edge states in a quantum spin-Hall system. *Physical review letters*, 101(24):246807, 2008.
- [36] M Wada, S Murakami, F Freimuth, and G Bihlmayer. Localized edge states in two-dimensional topological insulators: Ultrathin Bi films. *Physical Review B*, 83(12):121310, 2011.
- [37] Chen Fang, Matthew J Gilbert, Xi Dai, and B Andrei Bernevig. Multi-Weyl topological semimetals stabilized by point group symmetry. *Physical Review Letters*, 108(26):266802, 2012.
- [38] Chen Fang, Matthew J Gilbert, and B Andrei Bernevig. Bulk topological invariants in noninteracting point group symmetric insulators. *Physical Review B*, 86(11):115112, 2012.